

RESEARCH ARTICLE

10.1029/2018JA025611

Key Points:

- MMS observation of ion-scale flux ropes in the reconnection outflow region
- The initial X line is embedded in the exhaust region downstream of a second X line
- Flux transfer events (FTE) are formed between the two X lines due to tearing instability

Correspondence to:

K.-J. Hwang,
jhwang@swri.edu

Citation:

Hwang, K.-J., Sibeck, D. G., Burch, J. L., Choi, E., Fear, R. C., Lavraud, B., et al. (2018). Small-scale flux transfer events formed in the reconnection exhaust region between two X lines. *Journal of Geophysical Research: Space Physics*, 123, 8473–8488. <https://doi.org/10.1029/2018JA025611>






Received 25 APR 2018

Accepted 3 OCT 2018

Accepted article online 11 OCT 2018

Published online 29 OCT 2018

Small-Scale Flux Transfer Events Formed in the Reconnection Exhaust Region Between Two X Lines

K.-J. Hwang¹ , D. G. Sibeck² , J. L. Burch¹ , E. Choi¹ , R. C. Fear³ , B. Lavraud⁴ , B. L. Giles² , D. Gershman² , C. J. Pollock⁵ , J. P. Eastwood⁶ , Y. Khotyaintsev⁷ , Philippe Escoubet⁸, H. Fu⁹ , S. Toledo-Redondo¹⁰ , R. B. Torbert¹¹ , R. E. Ergun¹² , W. R. Paterson² , J. C. Dorelli² , L. Avanov^{2,13} , C. T. Russell¹⁴ , and R. J. Strangeway¹⁴ 

¹Southwest Research Institute, San Antonio, TX, USA, ²NASA Goddard Space Flight Center, Greenbelt, MD, USA, ³Physics and Astronomy, University of Southampton, Southampton, UK, ⁴Institut de Recherche en Astrophysique et Planétologie, CNRS, UPS, CNES, Université de Toulouse, Toulouse, France, ⁵Denali Scientific, LLC, Fairbanks, AK, USA, ⁶Imperial College, London, UK, ⁷Swedish Institute of Space Physics, Uppsala, Sweden, ⁸European Space Agency, Noordwijk, Netherlands, ⁹School of Space and Environment, Beihang University, Beijing, China, ¹⁰European Space Agency, ESAC, Madrid, Spain, ¹¹Space Science Center, University of New Hampshire, Durham, NH, USA, ¹²Laboratory for Atmospheric and Space Physics, University of Colorado Boulder, Boulder, CO, USA, ¹³The Goddard Planetary Heliophysics Institute, Baltimore, MD, USA, ¹⁴Institute of Geophysics and Planetary Physics, University of California, Los Angeles, CA, USA

Abstract We report MMS observations of the ion-scale flux transfer events (FTEs) that may involve two main X lines and tearing instability between the two X lines. The four spacecraft detected multiple isolated regions with enhanced magnetic field strength and bipolar B_n signatures normal to the nominal magnetopause, indicating FTEs. The currents within the FTEs flow mostly parallel to \mathbf{B} , and the magnetic tension force is balanced by the total pressure gradient force. During these events, the plasma bulk flow velocity was directed southward. Detailed analysis of the magnetic and electric field and plasma moments variations suggests that the FTEs were initially embedded within the exhaust region north of an X line but were later located southward/downstream of a subsequent X line. The cross sections of the individual FTEs are in the range of ~ 2.5 – 6.8 ion inertial lengths. The observations suggest the formation of multiple secondary FTEs. The presence of an X line in the exhaust region southward of a second X line results from the southward drift of an old X line and the reformation of a new X line. The current layer between the two X lines is unstable to the tearing instability, generating multiple ion-scale flux-rope-type secondary islands.

1. Introduction

Spacecraft crossing the Earth's magnetopause often observe a single transient structure or a series of bipolar signatures in the magnetic field component normal to the nominal magnetopause (B_n). Since Russell and Elphic (1978) termed this signature a flux transfer event (FTE), numerous studies of in situ observations (e.g., Paschmann et al., 1982; Sibeck & Siscoe, 1984) have determined typical FTE signatures, including either an increase or decrease in the magnetic field strength at (or bounding, in the case of crater FTEs) the center of the B_n reversal and an increase in the total pressure at the center of FTEs, where the pressure force balances the magnetic tension force (Ieda et al., 1998; Paschmann et al., 1982). FTEs detected inside the magnetosphere or the magnetosheath contain plasmas from both regions (Klumpar et al., 1990).

The various mechanisms for FTE generation invoke (1) transient bursts (spatially and temporally) of dayside reconnection (Russell & Elphic, 1978), (2) temporal modulation of the reconnection rate during continuous reconnection (Phan et al., 2004; Scholer, 1988; Southwood et al., 1988), or (3) multiple X lines (in 2-D representations) or separator lines (in 3-D representations; e.g., Hasegawa et al., 2010; Lee & Fu, 1985; Raeder, 2006; Scholer, 1995). These different generation mechanisms necessarily give rise to different magnetic topologies or magnetic field connectivities within and around the FTEs. Fear et al. (2008) categorized various flux rope models into three types: elbow-shaped flux-bundle FTEs, single X line FTEs, and multiple X line FTEs, corresponding to cases 1 to 3, respectively.

The elbow-shaped FTEs formed by localized patchy reconnection (Russell & Elphic, 1978) consist of a pair of flux tube bundles being peeled away from the reconnection site. Their magnetosheath and magnetospheric ends connect through a circular hole (with a diameter of $\sim 1 R_E$) on the magnetopause. This hole propagates

along the magnetopause away from the reconnection site in response to the combined effect of magnetic tension and pressure gradient forces. Having narrow azimuthal (dawn-dusk) extents, the flux ropes align with the magnetospheric/magnetosheath magnetic fields on either side of the magnetopause. The passage of the helical magnetic field lines within these flux ropes past a spacecraft results in the observed B_n . The spiral magnetic field lines connect the magnetosheath magnetic field to either the northern or southern high-latitude ionosphere. Bidirectional (hot and more isotropic) electrons are found at the edge of the flux rope (in the FTE core) while unidirectional ions may dominate the inner region of the FTE (Varsani et al., 2014).

Single X line FTEs are generated via transient increases in the reconnection rate. Enhanced thermal pressure within the exhaust region of newly reconnected magnetic field lines causes the events to bulge outward into the magnetosheath and magnetosphere as they move away from the reconnection line (Dunlop et al., 2005; Farrugia et al., 2011). This mechanism does not form a helical flux rope: instead, the newly reconnected magnetic field lines simply connect the magnetosheath to either the northern or southern hemisphere magnetospheric magnetic field. Single reconnection-line FTEs may contain a core guide field and can extend azimuthally over many Earth radii (R_E). Reconnection jets flow away from the X line on the edges of the events while thermalized plasmas populate within their core. The particle signatures within single X line FTEs should resemble those for FTEs formed by localized patchy reconnection since in both models the field lines are topologically open. Lockwood and Hapgood (1998) pointed out that the continuous variation in the ion distribution function between the magnetosheath-like high-pressure population at the event core, of which the field lines were reconnected earlier, and the surrounding magnetospheric populations on the draped field lines that were reconnected later corresponded to the evolution of reconnection and was consistent with the single X line model (not the elbow-shaped flux tube model).

The multiple X line scenario includes (1) a simultaneous in vivo (active) X line type where the edges of n FTEs are anchored between $n + 1$ separate X lines (Lee & Fu, 1985) and (2) a multiple sequential X line reconnection model where an old X line relocates providing an opportunity for a new X line to develop nearer to the subsolar magnetopause. Two ion jets converge toward the center of such FTEs. Together with the oppositely-directed jets, Hasegawa et al. (2010) reported heated magnetosheath electrons flowing both parallel and antiparallel to the magnetic field for a magnetosheath FTE, suggesting this behavior to be inconsistent with a single X line topology. However, mirroring of the heated plasma might explain the bidirectional electrons (Fear et al., 2007). Multiple X line FTEs exhibit mixed magnetic field topologies, for example, open field lines connecting the southern hemisphere to the magnetosheath, open field lines connecting the northern hemisphere to the magnetosheath, closed field lines connecting both hemispheres, and purely magnetosheath fields (Lee & Fu, 1985). Electron pitch angle distributions show energy-dependent variations that provide evidence for such diverse magnetic topologies (Pu et al., 2013; Zhong et al., 2013). Lindstedt et al. (2009) discussed multiple X lines forming along the magnetopause based on a broad density cavity with multiple dips observed in the separatrix region by Cluster.

The presence of guide fields distinguishes flux-rope type FTEs from two-dimensional magnetic islands. The relationship between guide fields and crater FTEs, across which the enhanced magnetic field strength (B) shows a central depression ("M"-shaped FTEs) with bipolar B_n perturbations, is unclear. Sibeck et al. (2008) reported more complicated structures where a region of B decrease bounds a B -enhanced core and the combined signatures are encircled by B increases at the periphery ("W"-shaped crater FTEs compared to M-shaped ones). Pressure pulses/waves of either external (solar wind) or internal (created within the magnetosheath) origin might cause a transient relocation of the spacecraft across the boundary layer (Sibeck & Smith, 1992) or with respect to an FTE, resulting in a crater-like variation in B . Owen et al. (2008) argued that a transient relocation of one spacecraft (C3) among the four Cluster spacecraft into the magnetosheath was explained by C3 crossing a region of eroded magnetic flux around a crater FTE. Farrugia et al. (2011) suggested that encounters with the separatrix may result in the crater-like B variations with bipolar B_n perturbations across the event.

Multispacecraft missions have advanced our understanding of the FTE structure, motion, and extent. Fear et al. (2008) used tetrahedral Cluster observations to describe an FTE with a much larger azimuthal than north-south extent, which is inconsistent with the elbow-shaped flux tube model. Dunlop et al. (2005) presented Cluster and TC-1 observations of a pair of FTEs propagating northward and southward away from the reconnection site, consistent with the single X line model. Hasegawa et al. (2010) reported THEMIS

observation of an FTE between two converging jets, and therefore suggested the event formed via multiple X line reconnection (e.g., Raeder, 2006). Øieroset et al. (2011) presented similar observations of bidirectional jets converging toward an FTE. Observations of electrons that were not trapped within the core of the event demonstrated that the event was three-dimensional and had an open magnetic field topology. Owen et al. (2001) used Cluster-FGM/PEACE observations to define the magnetic field connectivity of the substructure of FTEs inferred from the magnetic field and electron signatures. Farrugia et al. (2011) reported a single X line crater FTE with multiple layers on the basis of their magnetic, electric, and plasma signatures. Varsani et al. (2014) identified the multilayer interior and surrounding structures of a crater FTE based on the electron pitch angles using 125-ms observations of Cluster-PEACE measurements assuming that the electrons were gyrotropic. Øieroset et al. (2016) reported evidence for the existence of a reconnecting current sheet at the center of an FTE. Hasegawa et al. (2016) showed that a mesoscale (peak-to-peak B_n duration of <1 min) FTE formed during quasi-continuous multiple X line reconnection as indicated by ion flow and Hall magnetic field changes. Hwang et al. (2016) investigated the multilayered substructure of a macroscopic (with transverse scale side of $\sim 0.8 R_E$) FTE using ion and electron distribution functions. Zhou et al. (2017) reported an electron-scale current layer at the interface of two coalescing macroscopic (with sizes of $\sim 1 R_E$) flux ropes.

Previously reported magnetopause FTEs often have scale sizes comparable to one Earth radius (R_E). Drake et al. (2006) used particle-in-cell simulations to show the formation of secondary islands with only a few to several ion inertial length (d_i) scale sizes in the exhaust region during magnetic reconnection. They pointed out that stronger guide fields result in longer electron current sheets downstream from X lines. Longer electron current sheets are more likely to be unstable to secondary island formation. Huang et al. (2013) proposed a possible criterion to identify a secondary island by showing that the out-of-plane electron current in the secondary island is generated by the electrons accelerated by the reconnection electric field in the vicinity of an X line. The out-of-plane electron current is opposite to that in the primary island, which formed simultaneously with the appearance of the X line during guide-field reconnection. Eastwood et al. (2016) reported ion-scale (~ 7 ion inertial length radius) FTEs that were most likely generated by secondary reconnection and demagnetized ions observed by Magnetospheric Multiscale Mission (MMS). The Cluster measurements in the magnetotail (Wang et al., 2016) indicated that the reconnection ion diffusion region is filled with magnetic flux ropes that interact with neighboring flux ropes. Wang, Nakamura, Baumjohann, Russell, et al. (2017) presented MMS observations of three consecutive ion-scale FTEs to identify two neighboring FTEs that were coalescing, as evidenced by reconnection signatures shown in the current sheet between the two FTEs.

This paper proposes a new aspect in the generation mechanism for the ion-scale FTEs using MMS observations on 14 December 2015. The MMS spacecraft (Burch et al., 2015) were launched on 12 March 2015 and probed the Earth's dayside magnetopause in December 2015. We present MMS observations of small-scale (down to $\sim 2.5 d_i$) FTEs formed downstream of a reconnection X line. The four MMS spacecraft in their tetrahedral configuration were separated by ~ 15 – 21 km, which enabled us to explore the substructure of the FTEs including current densities and magnetic field curvature associated with the FTEs. Field and plasma flow signatures in and around the FTE indicate that the FTE was formed through a multiple X line process, in this case, a sequential process of an old X line drift and the reformation of a new X line formed along a magnetopause current sheet that was unstable to the tearing instability.

The following section briefly describes the MMS instruments used for the present study. An overview of the event in section 3 is followed by a description of its geometry and propagation characteristics in section 4. We then describe the detailed field and particle signatures (e.g., plasma moments and distributions, the current density, the magnetic curvature, and the electric field structures) related to reconnection in section 5, a presumed multiple X line FTE in section 6, and a series of ion-scale FTEs in section 7. We delineate a possible magnetic topology for the entire structure in section 8. Discussion and conclusions follow in section 9.

2. Instrumentation

The MMS spacecraft (Burch et al., 2015) fly in near-Earth-equatorial and highly elliptical orbits. The four MMS spacecraft are identically equipped with instruments including Fast Plasma Investigations (FPI; Pollock et al., 2016), magnetometers (FGM consisting of the digital fluxgate magnetometer (DFG) and the analogue magnetometer (AFG); Russell et al., 2014), and electric field instruments (EDP) consisting of the spin-plane double probe (SDP; Lindqvist et al., 2016) and the axial double probe (ADP; Ergun et al., 2014). We used the magnetic

field data from the digital fluxgate magnetometers (DFG) with a time resolution of 10 ms in burst mode, the DC electric field data calibrated from SDP and ADP (with a 0.122-ms time resolution in burst mode), and particle data in burst mode from the FPI/DIS for ions and FPI/DES for electrons with a 150- and 30-ms time resolution, respectively, a 11.25° angular resolution, and a ~10-eV–26-keV energy range (during December 2015).

3. Overview of the Event

On 14 December 2015, the barycenter of the MMS quartet, located near the prenoon dayside magnetopause slightly southward of the magnetic equator, was at [9.9, -4.3, -1.2] Earth radii (R_E) in Geocentric Solar Magnetospheric coordinates (GSM). Figure 1 shows the detailed field and plasma signatures from 0057:44 to 0100:14 UT, observed by MMS1.

The top panel (Figure 1a) shows the magnetic strength (black profiles) and the x (blue), y (green), and z (red) components of the magnetic field. The next four panels show the magnetic (\mathbf{B} ; Figure 1b) and electric (\mathbf{E} ; Figure 1c) field, and the ion (Figure 1d) and electron (Figure 1e) velocity in the LMN boundary coordinate system. We determined the LMN coordinates by employing minimum variance analysis (MVA) using the magnetic field data from the four MMS spacecraft (Paschmann & Daly, 1998) for the period of the nearest magnetopause crossing, 0117:10–0117:30 UT. Figure 2 shows ACE observations of the interplanetary magnetic field (IMF; Figure 2a) and solar wind velocity (Figure 2b). The vertical solid and dotted magenta lines indicate those parameters of the solar wind arriving at the Earth's magnetopause when MMS encountered the present event (Figure 1) and made the nearest magnetopause crossing, respectively. The IMF orientation is mostly antisunward and duskward, and slightly southward. During the ~18.3-min interval, no significant changes in the solar wind conditions are seen, providing confidence in the use of MVA on the nearest magnetopause crossing to determine the LMN frame. The derived LMN coordinates are $n = [0.84, -0.36, -0.41]$, $m = [-0.46, -0.87, -0.17]$, and $l = [0.30, -0.33, 0.89]$. The medium-to-minimum (maximum-to-medium) eigenvalue ratio from MVA is 15.0 (5.1), indicating a reliable calculation for the 10-ms time resolution data (Siscoe & Sney, 1972).

The ion number density (green in Figure 1f) is presented together with the ion total temperature (black). Figure 1g shows the plasma (red) and magnetic (blue) pressures, and the sum of plasma and magnetic pressures (black). The next three panels (Figures 1h–1j) show the l , m , and n components of the $\mathbf{E} \times \mathbf{B}$ drift (black) together with the ion (red) and electron (blue) velocities perpendicular to the magnetic field (\mathbf{B}). Figures 1k and 1l show current densities parallel and perpendicular to \mathbf{B} calculated from the curlometer technique (Dunlop et al., 2002) using \mathbf{B} (black) and estimated from plasma moments (magenta). Figure 1m displays the result of Walén tests; Figure 1n compares the ion bulk speed in the magnetopause current sheet frame (black) with the local Alfvén speed (magenta; discussion in section 5). Color-coded are the ion (Figure 1o) and electron (Figure 1p) energy spectrogram, and the pitch angle distributions of the low- (<100 eV), mid- (100 eV < energy < 1 keV), and high-energy (>1 keV) electrons (Figures 1q, 1r, and 1s, respectively).

At ~0058:13 UT (see the vertical dashed line marked by D at the top of Figure 1), MMS1 crossed from the low-latitude boundary layer (LLBL) where magnetospheric (e.g., >1-keV energy electrons) and magnetosheath (~100-eV electrons) plasmas coexist (Figure 1p) on magnetospheric field lines (positive B_z and B_l in Figures 1a and 1b) into a transitional region, termed the magnetopause boundary layer (MPBL). MPBL is populated mainly by bidirectional (more antiparallel than parallel) magnetosheath electrons (Figures 1p–1q) on the earthward side of the magnetopause (reduced positive B_z and B_l from those in LLBL; Figures 1a and 1b). At ~0058:36 UT (vertical dashed line B), MMS1 entered into a region of B_z (B_l) fluctuating around zero (Figures 1a and 1b) with enhanced fluxes of magnetosheath populations (Figures 1o–1q). These B_z (B_l) and particle signatures lead to the identification of this region as the magnetopause current sheet (MPCS).

Blue, green, and red bars at the top of Figure 1 indicate intervals when MMS observed the LLBL, MPBL, and MPCS, respectively. From the LLBL, passing through the MPBL, toward the MPCS, plasma densities (temperatures) increase (decrease; Figure 1f); plasma pressures are lower-than/balanced-with/larger-than magnetic pressures (Figure 1g). Within the MPCS electron pitch angle distributions are energy-dependent: low (mid-to-high) energy electrons are mostly counterstreaming (isotropic, perpendicular, or one-directional). In particular, we note a series of magnetic strength enhancements embedded in the current sheet (black profiles in Figure 1a and vertical magenta/blue shading in Figure 1). Bipolar changes in B_n during each magnetic hump

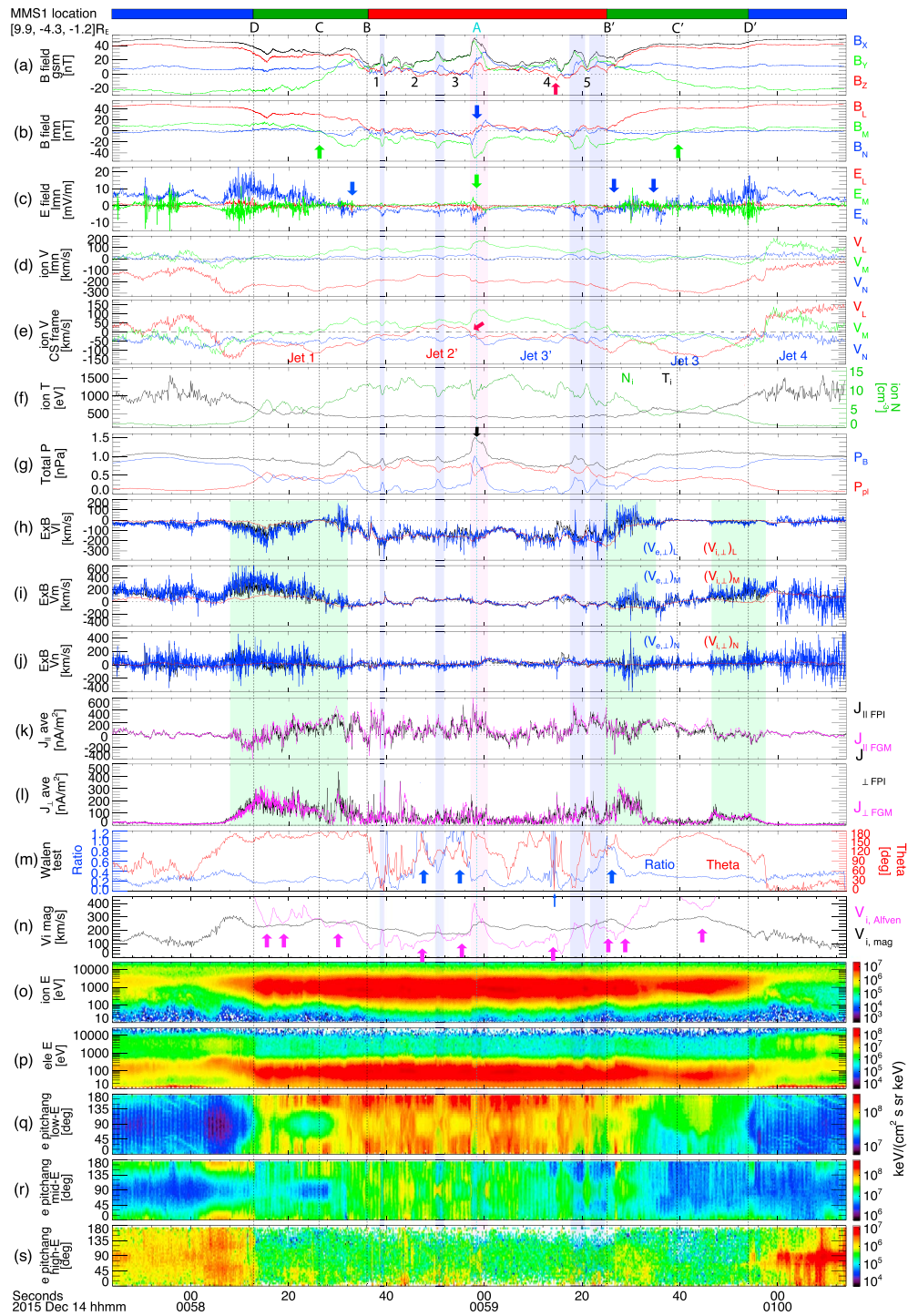


Figure 1. Overview of the magnetopause crossing by MMS1 (blue, green, red bars at the top of panels indicate intervals when MMS observed the LLBL, MPBL, and MPCs, respectively). (a) The magnetic strength (black profiles) and the x (blue), y (green), and z (red) components of the magnetic field in the GSM coordinates. The (b) magnetic (\mathbf{B}) and (c) electric (\mathbf{E}) field. The ion velocity (d) in the LMN boundary coordinate system and (e) in the central MPCs frame. (f) The ion number density (green) and total temperature (black). (g) The plasma (red) and magnetic (blue) pressures, presented with the sum of plasma and magnetic pressures (black). (h–j) The l , m , and n components of the $\mathbf{E} \times \mathbf{B}$ drift (black) together with the ion (red) and electron (blue) velocities perpendicular to \mathbf{B} . (k and l) The current densities parallel and perpendicular to \mathbf{B} calculated from the curlometer technique using \mathbf{B} (black) and estimated from plasma moments (magenta). (m) The result of Walén tests [the upstream magnetosheath reference are obtained from the data at $\sim 0059:14$ UT when B_z is most strongly southward, indicating the farthest spacecraft location into the magnetosheath; the running window is consistent with the sampling cadence of ion moments obtained from FPI/DIS (150 ms)]. (n) The ion bulk speed in the magnetopause current sheet frame (black) compared with the local Alfvén speed (magenta). The (o) ion and (p) electron energy spectrogram. The pitch angle distributions of the (q) low- (<100 eV), (r) mid- (100 eV $<$ energy $<$ 1 keV), and (s) high-energy (>1 keV) electrons, respectively.

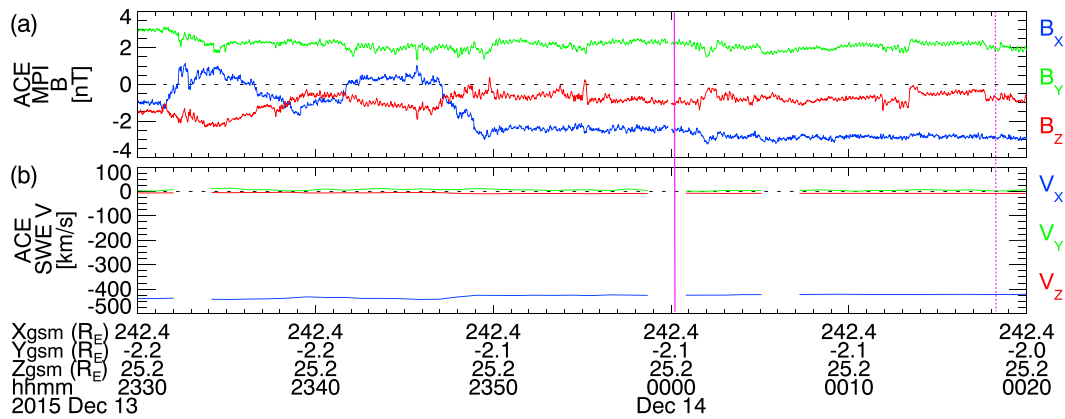


Figure 2. ACE observations of (a) interplanetary magnetic fields (IMF) and (b) solar wind velocities. The vertical solid and dotted magenta lines indicate times for the solar wind to arrive at the Earth’s magnetopause when MMS encountered the present event (Figure 1) and made the nearest magnetopause crossing, respectively.

(Figure 1b) suggest that these are a series of FTEs (details in section 6). Electron pitch angle distributions [in particular, mainly parallel low-energy electrons (Figure 1p)] also distinguish those transient structures from their peripheries in the MPCs (details in section 7). This suggests multiple magnetic topologies coexisting within the MPCs.

From ~0059:25 to 0059:54 UT, the spacecraft crossed a transition layer on magnetospheric field lines ($B'-D'$), similar to the prior MPBL ($D-B$). Both regions ($D-B$ and $B'-D'$) exhibit (1) asymmetric pitch angle distributions of low-energy magnetosheath electrons with more $90^\circ-180^\circ$ pitch angles than $0^\circ-90^\circ$ and (2) weak high-energy electron fluxes with more $0^\circ-90^\circ$ pitch angles (Figures 1q and 1s), indicating an open magnetic topology with a connection to the southern hemisphere. More unidirectional low-energy populations with $50^\circ-180^\circ$ pitch angles (Figure 1q) are observed in the later MPBL, $B'-D'$. The weaker $0^\circ-90^\circ$ pitch angle components seen in the initial MPBL, $D-B$, may represent magnetosheath-origin electrons that have been mirrored back from the ionosphere of the southern hemisphere. Their existence and/or intensity may indicate a time history of the magnetic field lines that underwent reconnection (details in section 9). After the short passage through this MPBL, MMS1 reentered the LLBL at ~0059:54 UT (D').

The magnetic and electric field and plasma parameters over the entire period shown in Figure 1 display symmetric patterns with respect to the center of the event period at ~0058:58 UT (the vertical cyan line), for example, B_z (B_l) ~40 nT initially, decreasing at ~0058:13 UT and dropping to around zero at ~0058:36 UT (Figures 1b and 1c). After fluctuating around zero, B_z (B_l) regains its positive value at ~0059:25 UT, and recovers to LLBL values at ~0059:54 UT. Likewise, the ion moments (Figures 1d and 1f) and the ion and electron energy spectrograms (Figures 1o and 1p) show the overall variation pattern mirrored with respect to the vertical cyan line. The overall MMS trajectory, therefore, had the following temporal sequence: LLBL, MPBL, MPCs, MPBL, and LLBL, consecutively.

During $D-B$ ($B'-D'$), B_m changed sign from positive to negative at ~0058:26 UT (from negative to positive at ~0059:39 UT) between the two step decreases (increases) in B_z (green arrows in Figure 1b; vertical dashed lines, C and C'). The dominant component of the electric field is along the n direction (Figure 1c). E_n is mostly positive during the both MPBL and becomes slightly negative around the MPCs (blue arrows in Figure 1c). These magnetic and electric fields are related to the reconnection Hall fields that are discussed in more details in sections 6 and 7. Within the MPCs ($B-B'$), B_m shows a background (non-FTE) value of ~ -10 nT, representing a guide field (section 9). The E_n is negative throughout the MPCs, mostly corresponding to the southward drift of the MPCs (section 4). The negative E_n becomes intense during each magnetic hump within the MPCs marked by blue/magenta shadings, which is detailed in section 7.

4. Local Normal and Propagation of Boundary Layers

To delineate the detailed structure and orientation of the boundaries between the LLBL and the MPBL (D and D'), within the MPBL (C and C'), and between the MPBL and the MPCs (B and B'), we performed MVA using the

Table 1

Boundary Normals at D to D' and Normal Propagation Vectors of B and B' in LMN ($\lambda_{\text{mid-min}}$ Is the Medium-To-Minimum Eigenvalue Ratio in the Minimum Variance Calculation)

	D	C	B	B'	C'	D'
Time (UT)	~00:58:13	~00:58:26	~00:58:36	~00:59:25	~00:59:39	~00:59:54
Normal in LMN coordinates	$\lambda_{\text{mid-min}} = 3.7$ [0.29, -0.06, 0.95]	$\lambda_{\text{mid-min}} = 11.5$ [0.64, -0.17, -0.75]	$\lambda_{\text{mid-min}} = 9.0$ [-0.81, -0.52, 0.27]	$\lambda_{\text{mid-min}} = 4.6$ [-0.78, 0.22, 0.58]	$\lambda_{\text{mid-min}} = 9.2$ [-0.19, -0.17, 0.97]	$\lambda_{\text{mid-min}} = 15.3$ [-0.21, 0.06, -0.98]
Normal propagation in LMN		$v = 129.2$ km/s [0.59, -0.49, -0.63]	$v = 225.3$ km/s [-0.99, -0.07, -0.12]	$v = 169.3$ km/s [-0.80, 0.08, 0.59]	$v = 63.8$ km/s [-0.38, -0.10, 0.92]	

magnetic field observations for each boundary crossing to determine a local boundary normal. The four spacecraft with an average separation of 17.4 km were almost in a tetrahedron enabling us to also estimate the normal propagation velocity of the MPCs and MPBL boundaries, C to C', via timing analysis (Paschmann & Daly, 1998). (B and B' are highly gradual relative to the spacecraft separation, giving rise to inaccuracies in timing.) We summarize the resulting local normals and propagation vectors in Table 1.

At the inner (closer to Earth) boundaries, D and D', the normals are primarily along the *n* direction. At the out-bound (toward the magnetosheath) and inbound (toward the magnetosphere) MPCs edges, B and B', (1) the normals have a significant *l* component; (2) both MVA-derived normals and four-spacecraft-timing-deduced normal propagation vectors qualitatively agree, indicating reliability of the minimum variance and timing analyses; and (3) both edges propagate mainly along the negative *l* direction, that is, southward. The initial outbound MPCs edge, B, with a negative V_l of ~223.0 km/s moves faster than the later inbound boundary, B', at $V_l \approx -135.4$ km/s. To demonstrate (3), we performed timing analyses at various locations of the MPCs between B and B' (marked by "1" to "5" in Figure 1a), by finding the timings that give the best correlation among the four spacecraft measurements of the magnetic field, combined with using specific features in the magnetic field profile. Table 2 shows the result. The southward or $-l$ component of the current sheet velocity is fastest close to B and gradually decreases toward B'.

5. Reconnection

The event is accompanied by negative V_l plasma flows (Figure 1d), that is, mostly southward jets, indicating MMS located within the outflow/exhaust region south of a reconnection X line (or X lines). The Walén relation (Sonnerup et al., 1981) identifies a current sheet boundary layer as a rotational discontinuity consistent with magnetic reconnection. The Walén test used here is $\mathbf{U}_{t2} - \mathbf{U}_{t1} = \pm \sqrt{\frac{1-\alpha_1}{\mu_0 \rho}} \left[\frac{1-\alpha_2}{1-\alpha_1} \mathbf{B}_{t2} - \mathbf{B}_{t1} \right]$, where $\Delta \mathbf{U}_t = \mathbf{U}_{t2} - \mathbf{U}_{t1}$ is the difference between the tangential components of the plasma velocity across the boundary; $\mathbf{B}_{t1,2}$ is the tangential component of the magnetic field; $\alpha = \mu_0(p_{\parallel} - p_{\perp})/B^2$ is the pressure anisotropy parameter; and the subscripts 1, 2 denote the two sides of the rotational discontinuity. We calculate $\Delta \mathbf{U}_{t, ob}$ and $\Delta \mathbf{U}_{t, th}$ corresponding to the left- and right-hand sides of the equation, respectively. The upstream magnetosheath conditions (reference, "1") are obtained from the data at ~0059:14 UT when B_z is most strongly southward, indicating the farthest spacecraft location into the magnetosheath (red arrow in Figure 1a).

Figure 1m illustrates the degree to which two quantities obey the Walén relationship: $R = |\Delta \mathbf{U}_{t, ob}| / |\Delta \mathbf{U}_{t, th}|$ (blue profiles in Figure 1m) and θ , the angle between $\Delta \mathbf{U}_{t, ob}$ and $\Delta \mathbf{U}_{t, th}$ in the plane tangential to the magnetopause (red). A perfect Walén test would give $R = 1$ and $\theta = 0^\circ$ or 180° for $B_n < 0$ and $B_n > 0$, respectively. Blue arrows mark intervals when the relationship is satisfied relatively well: within the MPCs and

Table 2

Normal Propagation Vectors of the MPCs at Multiple Locations in the LMN Coordinates

	Between B and 1	Between 1 and 2	Between 2 and 3	Between 3 and 4	Between 4 and 5
Time (UT)	~00:58:38	~00:58:46	~00:58:54	~00:59:13	~00:59:22
Normal propagation in LMN	$v = 213.4$ km/s [-0.89, 0.22, -0.39]	$v = 191.9$ km/s [-0.82, 0.18, 0.55]	$v = 183.9$ km/s [-0.90, 0.28, 0.33]	$v = 169.9$ km/s [-0.97, 0.16, -0.17]	$v = 133.5$ km/s [-0.96, 0.29, 0.06]

Note. The body text refers to the boldface column.

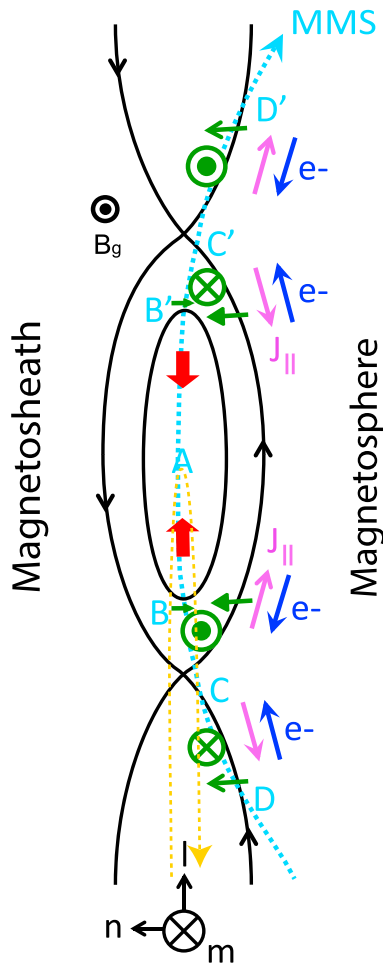


Figure 3. A simplified sketch illustrating a possible magnetic topology of a multiple X line-model FTE formed between two X lines. Dashed cyan and yellow arrows show presumed trajectories of the spacecraft relative to the FTE to compare MMS observations and expected observational features along these trajectories.

close to the inbound MPCCS edge (B'). The facts that $\theta \approx 170^\circ$ during D–B and $>90^\circ$ during $B'–D'$ are in accordance with the (slightly) increased B_x (Figure 1a) and enhanced southward jets (Figure 1d), as expected in an exhaust region southward of an X line and earthward of the reconnecting current sheet. However, the R value is <0.5 , possibly due to the imperfect magnetosheath reference associated with the complicated magnetic field topology. The ion bulk speed in the MPCCS proper close to the local Alfvén speed (magenta arrows in Figure 1n) still indicates ongoing reconnection. Large variations in both R and θ within the MPCCS also suggest a complicated/corrugated magnetic topology.

6. Magnetic Field Topology-1

The symmetry of the overall event across the vertical cyan dashed line (section 3) combined with the boundary normals and propagation vectors (section 4) and reconnection signatures (section 5; further discussion in this section) may lead to the interpretation of the observations in terms of a spacecraft trajectory encountering the magnetopause as shown in Figure 3. The schematic illustrates an FTE formed by multiple X line reconnection occurring northward and southward of the MPCCS ($B–B'$). The variability of the electron pitch angle distributions within the MPCCS (section 3) excludes an elbow-shaped FTE (Russell & Elphic, 1978) and a single X line model (Scholer, 1988; Southwood et al., 1988).

The ion bulk velocity (Figure 1d) show that (1) the bulk plasma flow is dominantly southward; (2) the southward flow velocity decreases in the MPCCS between B and B' ; and (3) across the center of the MPCCS, δV_i shows a positive to negative change around ~ -180 km/s. To emphasize (2) and (3), we use a reference frame that can relatively well represent the central MPCCS. Timing analysis for the MPCCS at $\sim 00:58:54$ UT near the center of the MPCCS (bold letters in Table 2) gives the propagation vector of 183.9 km/s $\times [-0.90, 0.28, 0.33]$ in LMN. The ion bulk velocity in this central MPCCS proper (Figure 1e) shows jet reversals ($V_i \approx \pm 40$ km/s at peaks) across the center of the FTE (red arrow). [Error estimates (Gershman et al., 2015) in V_i range $< 3.4\%$ (~ 7.8 km/s) during the MPCCS.] Counterstreaming flows toward the FTE center (red arrows in Figure 3) are a key characteristic of multiple-X line FTEs. The

general trend of the positive and then negative change of V_i also supports the MPCCS bounded by two X lines southward and northward of it. So either the observations (2) and (3) may support Figure 3, although the flow reversal is seen only in the MPCCS proper, or the schematic shown in Figure 3 cannot explain (1) the overall southward drift of the event. We further examine whether or not the detailed field and particle measurements support this speculation illustrated in Figure 3.

Asymmetric reconnection with no/moderate guide field ($<0.5 B_g$) leads the quadrupole Hall magnetic field (B_m) structure to be more bipolar and strong positive Hall electric fields (weakly negative E_n) to develop near the magnetospheric separatrices (in magnetospheric- and magnetosheath-side Hall regions adjacent to the current sheet; Mozer et al., 2008; Pritchett, 2008; Shay et al., 2016; Wang et al., 2017). During the outbound MPBL crossing, D–B, the positive-to-negative change in B_m and mainly positive E_n (Figures 1b and 1c) are, therefore, consistent with the Hall fields expected when a spacecraft traverses the southern-to-northern magnetospheric-side Hall region toward the current sheet (green arrows and symbols in the lower part of the illustration in Figure 3). The current density displays typical signatures of an ion diffusion region: (1) around D–B (green shades in Figure 1k) current densities parallel to \mathbf{B} ($J_{||}$) change sign from negative to positive, associated with current-carrying electrons streaming toward an X line in the southern and northern side of the X line, respectively (blue arrows in the lower part of Figure 3), as reported by Fujimoto et al. (1997) and Nagai et al. (2001) and predicted by Egedal et al. (2005, 2008; see magenta and blue arrows in the lower part

of Figure 3), and (2) enhanced perpendicular currents (Figure 1l) represent Hall currents (Sonnerup, 1979). Ion velocities perpendicular to \mathbf{B} (red profiles in Figures 1h–1j) significantly differ from the $\mathbf{E} \times \mathbf{B}$ drift (black) and electron velocities perpendicular to \mathbf{B} (blue), supporting an interpretation of MMS' crossing ion diffusion regions around C in the lower part of Figure 3. [The deviation between the ion and electron perpendicular velocities seen in the LLBL might come from different penetrations of the magnetosheath electrons and ions into the LLBL (Figures 1o and 1p) and/or the existence of the magnetospheric cold ions (Figure 1o)].

For the later (inbound) MPBL crossing, B'–D', ion perpendicular velocities again show notable disagreements with the $\mathbf{E} \times \mathbf{B}$ drift motion (green shading in Figures 1h–1j). Simultaneous intensification of perpendicular currents (Figure 1l) may represent Hall currents. If the spacecraft followed the inbound trajectory passing through the upper part of Figure 3, we would expect the repetition of the Hall field and J_{\parallel} variations as observed during the former MPBL crossing (D–B), that is, positive-to-negative B_m (with mostly positive E_n) and negative-to-positive J_{\parallel} around C' in Figure 3. However, B_m changes sign in the opposite manner to our expectation, that is, from negative to positive (Figure 1b), and J_{\parallel} shows an overall change in sign from positive to negative (Figure 1k). The magnetic geometry for the later, inbound MMS trajectory, therefore, needs a correction. We note that the consistently southward motion of the MPCS boundaries (B and B'; Table 1) as well as the central MPCS (A) excludes the possibility that the structures moved back and forth across the spacecraft (as illustrated by the yellow dashed arrow in Figure 3).

7. Multiple FTEs

To construct a more complete picture of the magnetic topology, we discuss substructures embedded within the MPCS. During the MPCS crossing (B–B'), the magnetic field strength shows multiple localized peaks denoted by magenta/blue shading (Figure 1a). The central one (the magenta shading from ~0058:57.0 to ~0059:00.9 UT) peaks at ~51 nT corresponding primarily to an increase in the positive B_y or negative B_m component (Figures 1a and 1b) from its background value of $B_m \sim -10$ nT, which represents the guide field; B_n changes sign from negative to positive across the vertical cyan dashed line at ~0058:58 UT (Figure 1b); here the trailing positive pulse/peak in the bipolar B_n is longer in duration than its negative counterpart, indicating an asymmetric shape, which is also seen in B_m profiles. These magnetic variations indicate that MMS traversed a southward moving FTE. Similar variations in the magnetic field attend each magnetic-flux hump (Figure 1a) marked with blue shading (during 0058:38.7–39.7, 0058:49.8–51.9, 0059:17.2–20.5, and 0059:21.4–24.8 UT).

Common features of those multiple transient structures include (1) enhanced negative E_n (Figure 1c) associated with the $\mathbf{E} \times \mathbf{B}$ motion propagating southward along the MPCS, (2) total pressure increases at the center of each structure (Figure 1g), (3) strong current density parallel to the local magnetic field, J_{\parallel} (Figure 1k), (4) energy-dependent electron pitch angle distributions: low-energy electrons are mostly antiparallel, mid-energy ones are either perpendicular or isotropic, and high-energy ones are mainly parallel at the strong core field at ~0058:39.1, 0058:50.5, 0058:58.1, 0059:18.4, and 0059:23.0 UT (Figures 1q–1s). Counterstreaming electrons of magnetosheath (low-energy; antiparallel) and magnetospheric (high-energy; parallel) origin indicate open magnetic topology with one end connected to the southern hemisphere. At the periphery of the FTEs, the pitch angle distributions of low-energy electrons are centered at 90° pitch angles. Further away from the FTEs, low-energy electrons are counterstreaming.

Figure 4 presents the MPCS crossing on an expanded time scale displaying physical quantities derived from the four spacecraft measurements (except Figure 4e): (a) the four-spacecraft averaged magnetic field components, B_x , B_m , and B_n (red, green, and blue profiles), together with the magnetic strength (black); (b) the angle between the four-spacecraft averaged magnetic field (Figure 4a) and the magnetic field measured at each satellite ($<15^\circ$ during multiple FTE observations); (c) the magnetic curvature, $(\mathbf{B} \cdot \nabla \mathbf{B})/\mu_0$; (d) the gradient of the total pressure, ∇P_{total} ; (e) the low-energy (<100 eV) electron pitch angle distribution from MMS1; (f) the four-spacecraft averaged current density calculated from plasma moments; (g) the electron velocity in the central MPCS frame; the current densities parallel (h) and perpendicular (i) to \mathbf{B} calculated from the curlometer technique using \mathbf{B} (black) and estimated from plasma moments (magenta); and (j–l) the l , m , and n components of the measured electric field (black), $-(\mathbf{V}_{\text{te}} \times \mathbf{B})$ (blue), $\mathbf{J} \times \mathbf{B}/ne$ (magenta), and $-\nabla \cdot \mathbf{P}_e/ne$ (cyan), where later three terms correspond to the motional/convective term, the Hall term, and the electron pressure term, respectively, in the generalized Ohm's law. Yellow profiles depict the sum of those terms for

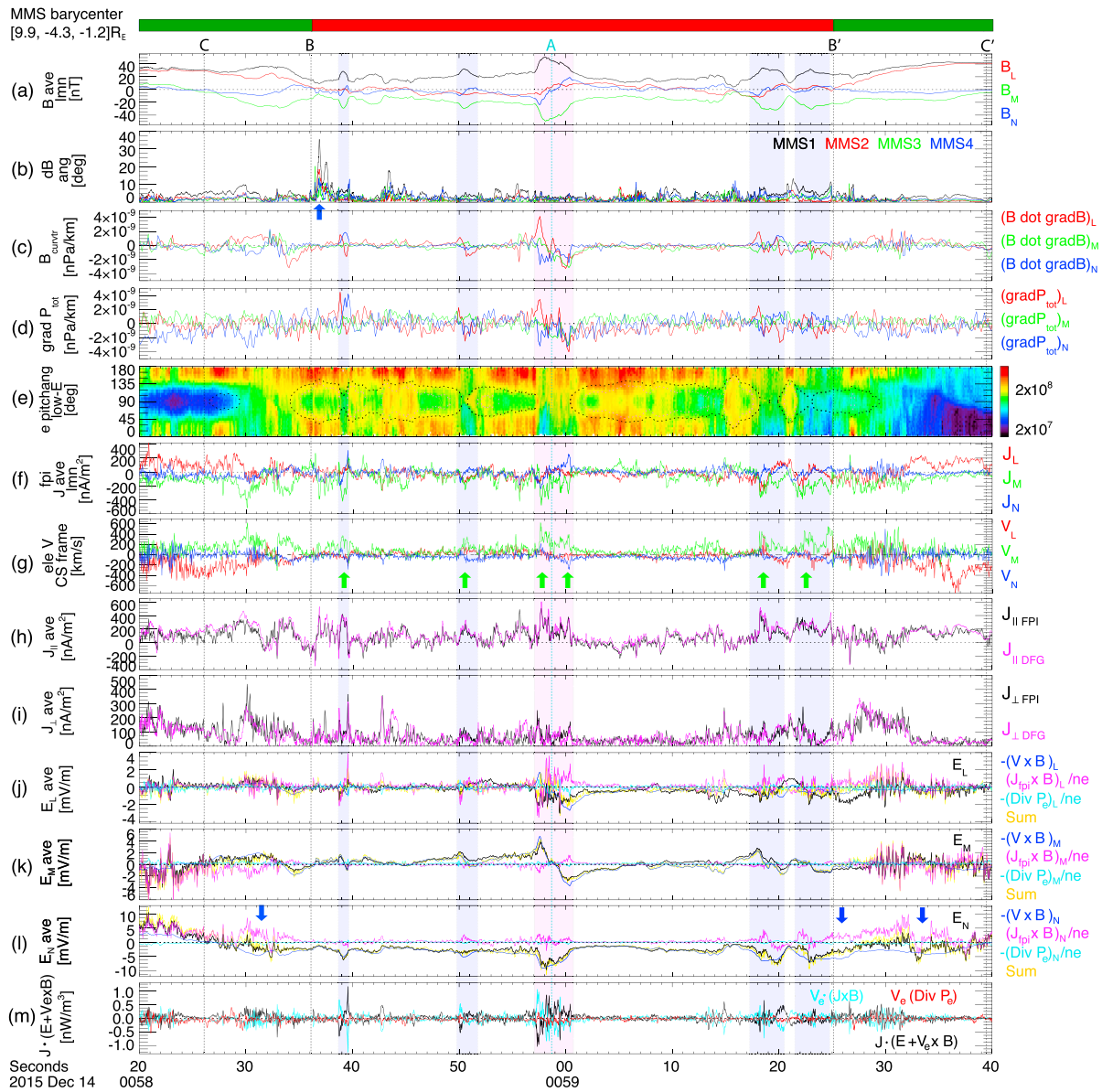


Figure 4. Expansion of the period of the MPCs crossing by MMS. (a) The four-spacecraft averaged magnetic field components, B_l , B_m , and B_n (red, green, and blue profiles), together with the magnetic strength (black). (b) The angle between the four-spacecraft averaged magnetic field and the magnetic field measured at each satellite. (c) The magnetic curvature $(\mathbf{B} \cdot \nabla \mathbf{B})/\mu_0$. (d) The gradient of the total pressure, ∇P_{total} . (e) The low-energy (<100 eV) electron pitch angle distribution from MMS1. (f) The four-spacecraft averaged current density calculated from plasma moments. (g) The electron velocity in the central MPCs frame. The current densities (h) parallel and (i) perpendicular to \mathbf{B} calculated from the curlometer technique using \mathbf{B} (black) and estimated from plasma moments (magenta). (j–l) The l , m , and n components of \mathbf{E} (black), $-(\mathbf{V}_e \times \mathbf{B})$ (blue), $\mathbf{J} \times \mathbf{B}/ne$ (magenta), and $-\nabla \cdot \vec{P}_e/ne$ (cyan), and the sum of the last three terms (yellow). (m) Joule dissipation in the electron frame, $\mathbf{J} \cdot \mathbf{E}' = \mathbf{J} \cdot (\mathbf{E} + \mathbf{V}_e \times \mathbf{B})$, compared with $\mathbf{V}_e \cdot (\mathbf{J} \times \mathbf{B})$, indicating energy transfer between magnetic and bulk kinetic energy (cyan) and $\mathbf{V}_e \cdot (\nabla \cdot \vec{P}_e)$ representing energy transfer between bulk kinetic and thermal energy (red). Green and red bars at the top of panels indicate intervals when MMS observed the LLBL and MPBL, respectively.

comparison with the measured electric field (black). Figure 4m shows Joule dissipation in the electron frame, $\mathbf{J} \cdot \mathbf{E}' = \mathbf{J} \cdot (\mathbf{E} + \mathbf{V}_e \times \mathbf{B})$, compared with $\mathbf{V}_e \cdot (\mathbf{J} \times \mathbf{B})$, indicating energy transfer between magnetic and bulk kinetic energy (cyan) and $\mathbf{V}_e \cdot (\nabla \cdot \vec{P}_e)$ representing energy transfer between bulk kinetic and thermal energy (red; Birn & Hesse, 2010).

During each transient feature (denoted as blue/magenta shading), the strong $J_{||}$ (Figure 4h) coincides with local enhancements in negative J_m (Figure 4f), the electric current along the core (axial) field of the

structure (Figure 4a). Away from the core region, perpendicular currents become dominant at the leading/trailing edges (Figure 4i). This is expected for a flux-rope type FTE. Figure 4c displays a series of isolated fluctuations in the magnetic curvature, showing one-to-one correspondence with the magnetic-flux humps (Figure 4a). The positive-to-negative change of the l component of the magnetic curvature during each transient (red profile in Figure 4c) represents the southern-to-northern portion of an FTE. The intermittent occurrence of these bipolar signatures can be interpreted as evidence for multiple (at least, five) southward moving FTEs. In a steady state FTE, the magnetic tension force directed toward the FTE center is balanced by the pressure gradient force pointing away from the center, $(\mathbf{B} \cdot \nabla \mathbf{B})/\mu_0 - \nabla P_{\text{total}} = 0$. The pressure gradient, ∇P_{total} (Figure 4d) demonstrates qualitative and reasonably quantitative (except the first feature detected at $\sim 0058:39$ UT) agreement with the magnetic curvature force (Figure 4c). These observations strongly indicate that the series of magnetic humps with bipolar B_n signatures are multiple quasi-steady state FTEs propagating southward along the MPCS, rather than the single large-scale FTE illustrated in Figure 3.

The low-energy electron pitch angle distributions within the MPCS and in the vicinity of these FTEs are interesting (Figure 4e). They indicate two populations: a mainly field-aligned, counterstreaming population and a population centered on 90° pitch angles. The two populations are well separated by the black and/or magenta dotted contours, which mark loss cone angles under an assumption that there is a mirror point with a magnetic strength of 30 nT (black) or 20 nT (magenta). The former population is parallel or antiparallel streaming electrons accelerated by the electrostatic parallel potential near the X line (Egedal et al., 2005, 2008). The latter is trapped electrons locally bouncing within the exhaust region with a large magnetic gradient/curvature associated with multiple FTEs, showing a pitch angle broadening at magnetic-strength minima in accordance with the first adiabatic invariant. The coexistence of these two populations has been reported in the near X line ion diffusion region (Lavraud et al., 2016). This is consistent with the ion-scale (section 9) MPCS undergoing reconnection.

The transverse (along the l direction) scale sizes of the five FTEs, inferred from the timing-analysis-deduced propagation velocity and durations of their passages (based on the peak-to-peak B_n signature) past MMS1, are $2.5 d_i$, $3.6 d_i$, $6.8 d_i$, $5.2 d_i$, and $5.9 d_i$, where d_i is the local ion inertial length (~ 75 km; here averaged over the MPCS crossing). These are therefore ion-scale FTEs. They feature large contributions from the Hall term, $\mathbf{J} \times \mathbf{B}/ne$ (magenta profiles in Figures 4j–4l) that balance the measured electric field [in particular, E_l (Figure 4j)]. The deviation of ion-perpendicular velocities from the $\mathbf{E} \times \mathbf{B}$ drift (mostly along l ; Figure 1h) also indicates a certain level of decoupling of ions from the magnetic field. We note that the electron pressure term (cyan in Figures 4j–4l) is often nonnegligible. However, the spacecraft separation, ~ 17.4 km, about 10 times larger than the electron inertial length (1.63 km in this case) would have entailed significant uncertainties in the pressure gradient calculation.

During the crossings of C–B and B'–C' within the outbound and inbound MPBL, E_n becomes mostly negative (blue arrows in Figure 4l corresponding to those in Figure 1c). Figure 4l shows that the E_n component is mostly balanced by the Hall term. This slightly negative E_n has been reported in both magnetospheric and magnetosheath-side Hall regions adjacent to the current sheet in asymmetric reconnection (e.g., Shay et al., 2016). During the MPCS (B–B'), the observed negative E_n and its enhancement during the FTEs (Figure 1c) are mostly contributed from the convection term, that is, southward drift of the MPCS and FTEs.

Lastly, we investigate the energy transfer occurring within/around the FTEs (Figure 4m). In the electron frame, the Joule heating ($\mathbf{J} \cdot \mathbf{E}'$; black) exhibits a negative, then positive dissipation pattern during each passage of the FTEs. This is particular evident for the first three FTEs. Comparing the energy transfer between the magnetic and bulk kinetic energies ($\mathbf{V}_e \cdot (\mathbf{J} \times \mathbf{B})$, cyan) and between the bulk kinetic and thermal energies ($\mathbf{V}_e \cdot (\nabla \cdot \vec{\mathbf{P}}_e)$, red), we find the relationship $\mathbf{J} \cdot \mathbf{E}' = -\mathbf{V}_e \cdot (\mathbf{J} \times \mathbf{B})$ holds across each FTE. The bulk kinetic energy is transferred to the field energy during the first half of the FTE crossings (on the southern sides of the FTEs) and vice versa during the second half of the crossings.

8. Magnetic Field Topology-2

Figure 5 illustrates a possible magnetic topology for the entire structure of the MPBL and MPCS encompassing the magnetic flux rope. Neither an elbow-shaped FTE (Russell & Elphic, 1978) or a single X line model (Scholer, 1988; Southwood et al., 1988) explains the variability of the electron pitch angle distributions

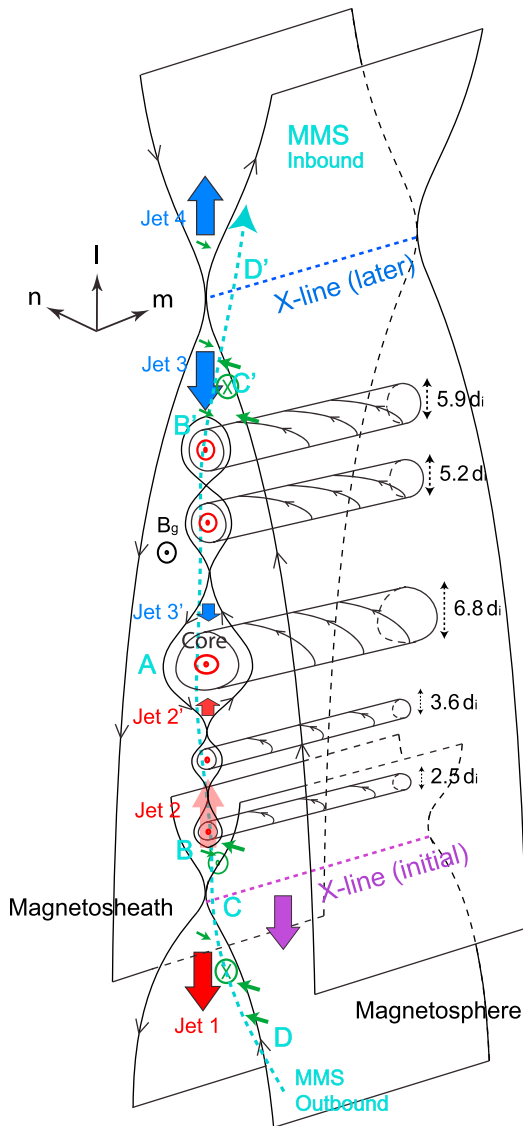


Figure 5. A schematic illustrating magnetic topology including small-scale flux ropes formed between the initial and new X lines in the frame of the MPCS, along which multiple FTEs are aligned. The initial X lines are located downstream of the second (later, dominant) X line. The cyan dashed arrow shows a possible path of the MMS spacecraft. Reconnection outflow jets, 1, 2', 3, 3', and 4 correspond to the MMS1 observations of V_I denoted in Figure 1e. At the MPCS proper, jet 2 decreases to jet 2' due to the relative motion of the initial X line (the violet arrow). Cyan letters, C, and C' correspond to the times when B_m and E_n change its sign. B (B') represent when the positive B_I decreases close to zero (increases from zero), that is, when the spacecraft enter (exit) the MPCS. The inferred cross-sectional scales of FTEs are shown in the ion inertial length (d_i).

with the distance from the FTE center and within the MPCS, which provides evidence for diverse magnetic topologies (Pu et al., 2013; Zhong et al., 2013). The absence of an overall flow reversal (the observation of mostly negative V_I) indicates that the spacecraft resided mainly on one side of the exhaust region (southward of the principal X line) throughout the interval studied. Invoking two reconnection X lines appending draped magnetic field lines to a single FTE (Figure 3) fails to explain the patterns of the Hall current and field variations (section 6) as well as a series of intermittent signatures of flux ropes (section 7) and the absence of oppositely directed reconnection jets between the two X lines without the MPCS-proper transformation.

Instead, mostly southward reconnection jets throughout the event indicate the presence of multiple reconnection X lines southward of a dominant X line as marked by "X line (later)" in Figure 5. Table 2 showed that the lower part of the MPCS [related to "X line (initial)"] moves southward faster than the upper part of the MPCS [X line (later)], indicating a relative drift between the two X lines, that is, the initial (southern) X line being pushed away by the southward outflow jet from the later (northern) X line. This figure explains most of the observational features: (1) southward flows (negative V_I) that maximize before entering and after exiting the MPCS [jets 1 and 3 in Figures 5 and 1e, during/around which reconnection Hall signatures are observed (green shadings in Figures 1h–1l) and section 6)]; (2) reconnection jet speeds comparable to local Alfvén speeds, that is, the Walén relation holds (Figures 1m and 1n and section 5); (3) detailed B_m and E_n profiles consistent with expected Hall fields (green arrows and symbols in Figure 5); (4) a weak flow reversal across the central flux rope (Figure 1e; jets 2' and 3' in Figures 5 and 1e; note that in the central MPCS proper, jet 2 is measured as jet 2' due to the faster southward motion of the presumed initial X line); (5) unidirectional (perpendicular, counter-streaming) low-energy electrons in the core of (on the close periphery of, further away from) the central FTE (Figures 1q and 2e and section 7), providing evidence for diverse magnetic topologies and the MPCS undergoing reconnection; and (6) intermittent periods of flux rope signatures with positive-to-negative transitions in the I component of the magnetic curvature indicating the southern-to-northern passage of FTEs [Figure 4c; positive (negative) n components indicating MMS crossing of the magnetospheric (magnetosheath) side of the FTEs, as depicted in Figure 5].

During jet 4 observed from ~0059:58 to 0100:14 UT (Figure 1e), the Hall current signatures are rather unclear (Figures 1k and 1l). The rapid change in V_I in the MPCS proper from negative (jet 3) to positive (jet 4) values around D' (Figure 1e) might suggest that jet 4 is northward outflow jets from the new (later) X line. Points (1) to (5) indicate that there were at least two active X lines during the event. The appearance of a series of flux ropes suggests that the MPCS anchored at the two X lines was unstable to the tearing mode, leading to the formation of multiple secondary islands or flux ropes, to be discussed in the following section.

9. Discussion and Conclusions

In this paper, we report a series of flux ropes that formed between two reconnection X lines observed by the MMS mission. The southward reconnection jets throughout the event indicate that a reconnection X line located southward of another X line was embedded downstream of the second X line. The cross sections of the flux ropes range from 2.5 d_i to 6.8 d_i (or 27.1 d_i including the region of draped

magnetic fields around the central flux rope, A). These ion-scale FTEs are characterized by large contributions from the Hall term, $\mathbf{J} \times \mathbf{B}/ne$ in balancing the measured electric field (Figures 4i–4k), consistent with Eastwood et al. (2016).

The overall magnetic topology appears consistent with predictions for the so-called “sequential multiple X line reconnection (SMXR) model” proposed by Raeder (2006). This model premises that an initial reconnection X line forms slightly southward of the flow stagnation point in the subsolar region and thus moves southward along the magnetopause. Subsequently, a new X line forms near the location of the initial X line, resulting in the formation of a magnetic flux rope between the two X lines.

The SMXR process can explain the appearance of an X line downstream from another X line via the drift of an old X line and the reformation of a new X line near the location of the initial X line. The initial (later) MPBL, D–B ($B'–D'$) exhibited the coexistence (absence/rarefaction) of the low-energy electrons with $0^\circ–90^\circ$ pitch angles (Figure 1q). This relatively parallel component may represent magnetosheath electrons mirrored from the southern hemisphere ionosphere. Then, the difference in the parallel component intensity between the two MPBL may indicate a time history of the reconnected magnetic field: the initial MPBL around an old X line enabled a portion of the magnetosheath electrons that have been penetrated into the magnetosphere due to reconnection to be mirrored back and observed there while the later MPBL around a new X line mainly corresponds to newly reconnected magnetic fields on which penetrating electrons dominate. This interpretation is consistent with the SMXR scenario.

The SMXR model predicts that FTEs occur more frequently in summer/winter (when the Earth’s dipole tilt is larger) and the FTEs propagate into the winter hemisphere. This has been supported observationally by Korotova et al. (2008); Fear, Milan, et al. (2012); and Fear, Palmroth, et al. (2012). Previous in situ observations suggestive of the SMXR-driven FTEs (e.g., Hasegawa et al., 2010; Zhang et al., 2008) estimated their transverse width to be ~ 0.8 to several R_E . The present event was observed southward of the magnetic equator. Here the reconnecting current sheet moved southward. The leading edge of the current sheet (indicative of the initial X line motion) propagated southward faster than the trailing edge of the current sheet (indicative of the new X line motion), consistent with the X line drift and reformation scenario. The FTEs also moved southward, *however, into the summer hemisphere*. These are small-scale FTEs with sizes down to ion scales, which may lead to a difference from the prediction for the SMXR FTEs with sizes on the order of R_E .

Whether the small-scale flux ropes in series were preexisting along the magnetopause before the two main X lines formed or they resulted from reconnection processes initiated at the two X lines remains unclear. The scale sizes of the FTEs with a few to several d_i lengths might suggest that they are likely to be secondary islands formed in the reconnection exhaust region, first predicted by Drake et al. (2006) using full-particle simulation codes. They emphasized that a strong guide field leading to the extended electron current sheet downstream of the X line facilitates the formation of secondary islands. The MMS spacecraft measured significant background $+B_y$ ($B_m \sim -10$ nT) components during their crossing of the MPCs, indicating component reconnection with a guide field, $B_g \sim 0.2 B_0$, where $B_0 \sim 50$ nT represents the magnetic field strength in the LBL.

Huang et al. (2013) used particle-in-cell simulations of the symmetric current sheet to show that the out-of-plane electron current in the secondary island is opposite to that in the primary island. The former along the $+y$ direction in their simulation domain ($-m$ direction in the dayside reconnection) was mostly generated by the accelerated electrons by the reconnection electric field in the vicinity of an X line, while the latter along the $-y$ ($+m$) direction is related to the acceleration of the trapped electron due to the compression of the island. In the asymmetric case of dayside reconnection, the Hall electric field (E_n) is found to primarily cause the $-y$ (m) directional electron-meandering motion adjacent to an X line (e.g., Bessho et al., 2016; Shay et al., 2016). Figure 4g shows strong out-of-plane electron flows along the m direction within the multiple FTEs. Enhancements of those electron jets (marked by green arrows) coincide with peaks in J_{\parallel} (Figure 4h) or negative J_m (Figure 4f) and enhancements in E_n (Figure 4l), consistent with the prediction by Huang et al. (2013), in the asymmetric current sheet.

Eastwood et al. (2016) reported that the secondary islands exhibit filamentary currents. Wang, Nakamura, Baumjohann, Russell, et al. (2017) proposed that the current inside the flux ropes detected in the exhaust region southward of a dayside reconnection X line are largely dynamic, fragmenting with time. We find

similar fragmented currents within the series of FTEs (except the second one at $\sim 0058:50.5$ UT; Figure 4h). Those subion-scale ($\leq \sim d_i$) filamentary currents are mainly carried by electron jets in the m direction [Figure 4g; $J_r \sim -0.28 J_e$ (not shown)].

The relative drift velocity between the presumed initial (faster) and later X lines (Table 2) might have elongated the current sheet to become tearing-unstable. To test whether or not the criteria for the tearing instability were met (Coppi et al., 1966; Furth et al., 1963), we estimated the thickness (Δ) of the current sheet from the spacecraft separation along the n direction (taken during the short time period from 0058:36.9–37.0 UT, marked by a blue arrow in Figure 4b, when the four spacecraft positioned well separately across the current sheet based on B_y) and, then, by fitting the four-point magnetic field variations to a Harris model (Harris, 1962; Hwang et al., 2013). The model yields $\Delta = 119$ km ($1.58 d_i$). We assume that the cross-sectional scales of the central FTE including draped fields ($27.1 d_i$) are an estimate of the wavelength (λ) of the initial mode. This estimate satisfies the instability criterion, $k\Delta (=0.37) \leq 1$, where $k (=2\pi/\lambda)$ is the wave number associated with the spacing along l of the inferred tearing-mode structure.

The overview trajectory of MMS departing the magnetopause, entering the MPCS, and then returning to the magnetosphere may indicate transient compression of the dayside magnetopause. The mostly Parker-spiral IMF orientation (Figure 2) and the MMS location at the prenoon magnetopause ($[9.9, -4.3, -1.2] R_E$) suggest that the event may have occurred in response to density or dynamic pressure variations generated near the quasi-parallel bow shock. Such density or dynamic pressure enhancements can locally compress the magnetopause (e.g., Sibeck et al., 1989). Without in situ measurements of near bow shock or ~ 1 -min period fluctuations corresponding to the MMS event in high-latitude ground magnetograms near locations magnetically conjugate to the MMS for the present event, and in the absence of any clear V_n signatures around the MPCS (Figure 1d), we cannot be sure that the entry into the MPCS was caused by a transient compression of the magnetopause. However, if it was, then bow shock generated structures or fluctuations might have compressed the magnetopause between the two X lines to the point where it was thin enough to excite the tearing instability.

Therefore, we conclude that the observational indications of multiple X lines where the southward X line was in the exhaust region downstream of the northward X line could result from the sequential process of the old X line drift and the reformation of a new X line. The magnetopause current layer between the two X lines could have been unstable to the tearing instability, generating multiple ion-scale flux-rope-type secondary islands. This event is similar to secondary island-type FTEs reported by Eastwood et al. (2016) and Wang, Nakamura, Baumjohann, Russell, et al. (2017); in that, their generation invokes secondary reconnection processes and the ion demagnetization and filamentary currents are observed. The present event also shows a good agreement with Huang et al. (2013); in that, the out-of-plane electron current in the secondary island is mostly generated by the near-X line reconnection process. The scale sizes of FTEs in the present event (up to $6.8 d_i$ down to $2.5 d_i \sim 187.5$ km) are less than secondary islands reported by Eastwood et al. (2016; $7 d_i \sim >1,000$ km) and comparable to those reported by Wang, Nakamura, Baumjohann, Russell, et al. (2017) ($1.3\text{--}8.6 d_i$; $91\text{--}609$ km). The generation mechanism of the present FTEs may involve two main SMXR-type X lines and tearing instability between the two X lines.

Acknowledgments

This study was supported, in part, by NASA's MMS project at the Goddard Space Flight Center; NSF AGS-1305374 and AGS-1602510; NASA NNX16AI39G/80NSSC18K1534, 80NSSC18K0570, and 80NSSC18K0693; and ISSI program: MMS and Cluster observations of magnetic reconnection. MMS data sets were provided by the MMS science working group teams through the link <http://lasp.colorado.edu/mms/sdc/public/>. We acknowledge MMS FPI and field teams for providing data. K.J.H. thanks the EPD team, Misha Sitnov for the useful discussions, and all the members of the MMS instruments and Modeling/Theory team. R.C.F. was supported by Science and Technology Facilities Council (STFC) Ernest Rutherford Fellowship ST/K004298/2. J. P.E. was funded by STFC (UK) grant ST/N000692/1.

References

- Bessho, N., Chen, L.-J., & Hesse, M. (2016). Electron distribution functions in the diffusion region of asymmetric magnetic reconnection. *Geophysical Research Letters*, *43*, 1828–1836. <https://doi.org/10.1002/2016GL067886>
- Birn, J., & Hesse, M. (2010). Energy release and transfer in guide field reconnection. *Physics of Plasmas*, *17*(1), 012109. <https://doi.org/10.1063/1.3299388>
- Burch, J. L., Moore, T. E., Torbert, R. B., & Giles, B. L. (2015). Magnetospheric Multiscale overview and science objectives. *Space Science Reviews*, *199*(1–4), 5–21. <https://doi.org/10.1007/s11214-015-0164-9>
- Coppi, B., Laval, G., & Pellat, R. (1966). Dynamics of the geomagnetic tail. *Physical Review Letters*, *16*(26), 1207–1210. <https://doi.org/10.1103/PhysRevLett.16.1207>
- Drake, J. F., Swisdak, M., Schoeffler, K. M., Rogers, B. N., & Kobayashi, S. (2006). Formation of secondary islands during magnetic reconnection. *Geophysical Research Letters*, *33*, L13105. <https://doi.org/10.1029/2006GL025957>
- Dunlop, M., Balogh, A., Glassmeier, K.-H., & Robert, P. (2002). Four-point cluster application of magnetic field analysis tools: The Curlometer. *Journal of Geophysical Research*, *107*(A11), 1384. <https://doi.org/10.1029/2001JA005088>
- Dunlop, M. W., Taylor, M. G. G. T., Davies, J. A., Owen, C. J., Pitout, F., Fazakerley, A. N., et al. (2005). Coordinated cluster/double star observations of dayside reconnection signatures. *Annales de Geophysique*, *23*(8), 2867–2875. <https://doi.org/10.5194/angeo-23-2867-2005>
- Eastwood, J. P., Phan, T. D., Cassak, P. A., Gershman, D. J., Haggerty, C., Malakit, K., et al. (2016). Ion-scale secondary flux ropes generated by magnetopause reconnection as resolved by MMS. *Geophysical Research Letters*, *43*, 4716–4724. <https://doi.org/10.1002/2016GL068747>

- Egedal, J., Fox, W., Porkolab, M., Øieroset, M., Lin, R. P., Daughton, W., & Drake, J. F. (2008). Evidence and theory for trapped electrons in guide field magnetotail reconnection. *Journal of Geophysical Research*, *113*, A12207. <https://doi.org/10.1029/2008JA013520>
- Egedal, J., Øieroset, M., Fox, W., & Lin, R. P. (2005). In situ discovery of an electrostatic potential, trapping electrons and mediating fast reconnection in the Earth's magnetotail. *Physical Review Letters*, *115*(A3), 025006. <https://doi.org/10.1103/PhysRevLett.94.025006>
- Ergun, R. E., Tucker, S., Westfall, J., Goodrich, K. A., Malaspina, D. M., Summers, D., et al. (2014). The axial double probe and fields signal processing for the MMS mission. *Space Science Reviews*, *199*(1-4), 167–188. <https://doi.org/10.1007/s11214-014-0115-x>
- Farrugia, C. J., Chen, L. J., Torbert, R. B., Southwood, D. J., Cowley, S. W. H., Vrubleviskis, A., et al. (2011). "Crater" flux transfer events: Highroad to the X line? *Journal of Geophysical Research*, *116*, A02204. <https://doi.org/10.1029/2010ja015495>
- Fear, R. C., Milan, S. E., Fazakerley, A. N., Lucek, E. A., Cowley, S. W. H., & Dandouras, I. (2008). The azimuthal extent of three flux transfer events. *Annales de Geophysique*, *26*(8), 2353–2369. <https://doi.org/10.5194/angeo-26-2353-2008>
- Fear, R. C., Milan, S. E., Fazakerley, A. N., Owen, C. J., Asikainen, T., Taylor, M. G. T., et al. (2007). Motion of flux transfer events: A test of the cooling model. *Annales de Geophysique*, *25*(7), 1669–1690. <https://doi.org/10.5194/angeo-25-1669-2007>
- Fear, R. C., Milan, S. E., & Oksavik, K. (2012). Determining the axial direction of high-shear flux transfer events: Implications for models of FTE structure. *Journal of Geophysical Research*, *117*, A09220. <https://doi.org/10.1029/2012JA17831>
- Fear, R. C., Palmroth, M., & Milan, S. E. (2012). Seasonal and clock angle control of the location of flux transfer event signatures at the magnetopause. *Journal of Geophysical Research*, *117*, A04202. <https://doi.org/10.1029/2011JA017235>
- Fujimoto, M., Nakamura, M. S., Shinohara, I., Nagai, T., Mukai, T., Saito, Y., et al. (1997). Observations of earthward streaming electrons at the trailing boundary of a plasmoid. *Geophysical Research Letters*, *24*(22), 2893–2896. <https://doi.org/10.1029/97GL02821>
- Furth, H. P., Kilean, K., & Rosenbluth, M. N. (1963). Finite-resistivity instabilities of a sheet pinch. *Physics of Fluids*, *6*(4), 459. <https://doi.org/10.1063/1.1706761>
- Gershman, D. J., Dorelli, J. C., Viñas, A. F., & Pollock, C. J. (2015). The calculation of moment uncertainties from velocity distribution functions with random errors. *Journal of Geophysical Research: Space Physics*, *120*, 6633–6645. <https://doi.org/10.1002/2014JA020775>
- Harris, E. G. (1962). On a plasma sheet separating regions of oppositely directed magnetic field. *Nuovo Cimento*, *23*(1), 115–121. <https://doi.org/10.1007/BF02733547>
- Hasegawa, H., Kitamura, N., Saito, Y., Nagai, T., Shinohara, I., Yokota, S., et al. (2016). Decay of mesoscale flux transfer events during quasi-continuous spatially extended reconnection at the magnetopause. *Geophysical Research Letters*, *43*, 4755–4762. <https://doi.org/10.1002/2016GL069225>
- Hasegawa, H., Wang, J., Dunlop, M. W., Pu, Z. Y., Zhang, Q. H., Lavraud, B., et al. (2010). Evidence for a flux transfer event generated by multiple X-line reconnection at the magnetopause. *Geophysical Research Letters*, *37*, L16101. <https://doi.org/10.1029/2010GL044219>
- Huang, C., Lu, Q., Wu, M., Lu, S., & Wang, S. (2013). Out-of-plane electron currents in magnetic islands formed during collisionless magnetic reconnection. *Journal of Geophysical Research: Space Physics*, *118*, 991–996. <https://doi.org/10.1002/jgra.50185>
- Hwang, K.-J., Goldstein, M. L., Wendel, D. E., Fazakerley, A. N., & Gurgiolo, C. (2013). Cluster observations near reconnection X lines in Earth's magnetotail current sheet. *Journal of Geophysical Research: Space Physics*, *118*, 4199–4209. <https://doi.org/10.1002/jgra.50403>
- Hwang, K.-J., Sibeck, D. G., Giles, B. L., Pollock, C. J., Gershman, D., Avakov, L., et al. (2016). The substructure of a flux transfer event observed by the MMS spacecraft. *Geophysical Research Letters*, *43*, 9434–9443. <https://doi.org/10.1002/2016GL070934>
- Ieda, A., Machida, S., Mukai, T., Saito, Y., Yamamoto, T., Nishida, A., et al. (1998). Statistical analysis of plasmoid evolution with Geotail observations. *Journal of Geophysical Research*, *103*(A3), 4453–4465. <https://doi.org/10.1029/97JA03240>
- Klumpar, D. M., Fuselier, S. A., & Shelley, E. G. (1990). Ion composition measurements within magnetospheric flux transfer events. *Geophysical Research Letters*, *17*(13), 2305–2308. <https://doi.org/10.1029/GL0171013p02305>
- Korotova, G. I., Sibeck, D. G., & Rosenberg, T. (2008). Seasonal dependence of Interball flux transfer events. *Geophysical Research Letters*, *35*, L05106. <https://doi.org/10.1029/2008GL033254>
- Lavraud, B., Zhang, Y. C., Vernisse, Y., Gershman, D. J., Dorelli, J., Cassak, P. A., et al. (2016). Currents and associated electron scattering and bouncing near the diffusion region at Earth's magnetopause. *Geophysical Research Letters*, *43*, 3042–3050. <https://doi.org/10.1002/2016GL068359>
- Lee, L. C., & Fu, Z. F. (1985). A theory of magnetic flux transfer at the Earth's magnetopause. *Geophysical Research Letters*, *12*(2), 105–108. <https://doi.org/10.1029/GL012i002p00105>
- Lindqvist, P.-A., Olsson, G., Torbert, R. B., King, B., Granoff, M., Rau, D., et al. (2016). The spin-plane double probe electric field instrument for MMS. *Space Science Reviews*, *199*(1-4), 137–165. <https://doi.org/10.1007/s11214-014-0116-9>
- Lindstedt, T., Khotyaintsev, Y. V., Vaivads, A., Andre, M., Fear, R. C., Lavraud, B., et al. (2009). Separatrix regions of magnetic reconnection at the magnetopause. *Annals of Geophysics*, *27*(10), 4039–4056. <https://doi.org/10.5194/angeo-27-4039-2009>
- Lockwood, M., & Haggood, M. A. (1998). On the cause of a magnetospheric flux transfer event. *Journal of Geophysical Research*, *103*(A11), 26,453–26,478. <https://doi.org/10.1029/98JA02244>
- Mozer, F. S., Angelopoulos, V., Bonnell, J., Glassmeier, K. H., & McFadden, J. P. (2008). THEMIS observations of modified hall fields in asymmetric magnetic field reconnection. *Geophysical Research Letters*, *35*, L17504. <https://doi.org/10.1029/2007GL033033>
- Nagai, T., Shinohara, I., Fujimoto, M., Hoshino, M., Saito, Y., Machida, S., & Mukai, T. (2001). Geotail observations of the hall current system: Evidence of magnetic reconnection in the magnetotail. *Journal of Geophysical Research*, *106*(A11), 25,929–25,949. <https://doi.org/10.1029/2001JA900038>
- Øieroset, M., Phan, T. D., Eastwood, J. P., Fujimoto, M., Daughton, W., Shay, M. A., et al. (2011). Direct evidence for a three-dimensional magnetic flux rope flanked by two active magnetic reconnection X-lines at Earth's magnetopause. *Physical Review Letters*, *107*(16), 165007. <https://doi.org/10.1103/PhysRevLett.107.165007>
- Øieroset, M., Phan, T. D., Haggerty, C., Shay, M. A., Eastwood, J. P., Gershman, D. J., et al. (2016). MMS observations of large guide field symmetric reconnection between colliding reconnection jets at the center of a magnetic flux rope at the magnetopause. *Geophysical Research Letters*, *43*, 5536–5544. <https://doi.org/10.1002/2016GL069166>
- Owen, C. J., Fazakerley, A. N., Carter, P. J., Coates, A. J., Krauklis, I. C., Szita, S., et al. (2001). Cluster PEACE observations of electrons during magnetospheric flux transfer events. *Annales de Geophysique*, *19*(10/12), 1509–1522. <https://doi.org/10.5194/angeo-19-1509-2001>
- Owen, C. J., Marchaudon, A., Dunlop, M. W., Fazakerley, A. N., Bosqued, J. M., Dewhurst, J. P., et al. (2008). Cluster observations of "crater" flux transfer events at the dayside high-latitude magnetopause. *Journal of Geophysical Research*, *113*, A07S04. <https://doi.org/10.1029/2007ja012701>
- Paschmann, G., & Daly, P. W. (1998). *Analysis methods for multispacecraft data* (Sci. Rep. 001). Bern: International Space Science Institute.
- Paschmann, G., Haerendel, G., Papamastorakis, I., Sckopke, N., Bame, S. J., Gosling, J. T., & Russell, C. T. (1982). Plasma and magnetic-field characteristics of magnetic-flux transfer events. *Journal of Geophysical Research*, *87*(A4), 2159–2168. <https://doi.org/10.1029/JA087iA04p02159>

- Phan, T. D., Dunlop, M. W., Paschmann, G., Klecker, B., Bosqued, J. M., Rème, H., et al. (2004). Cluster observations of continuous reconnection at the magnetopause under steady interplanetary magnetic field conditions. *Annales de Geophysique*, 22(7), 2355–2367. <https://doi.org/10.5194/angeo-22-2355-2004>
- Pollock, C., Moore, T., Jacques, A., Burch, J., Gliese, U., Saito, Y., et al. (2016). Fast plasma investigation for Magnetospheric Multiscale. *Space Science Reviews*, 199(1–4), 331–406. <https://doi.org/10.1007/s11214-016-0245-4>
- Pritchett, P. L. (2008). Collisionless magnetic reconnection in an asymmetric current sheet. *Journal of Geophysical Research*, 113, A06210. <https://doi.org/10.1029/2007JA012930>
- Pu, Z. Y., Raeder, J., Zhong, J., Bogdanova, Y. V., Dunlop, M., Xiao, C. J., et al. (2013). Magnetic topologies of an in vivo FTE observed by double star/TC-1 at Earth's magnetopause. *Geophysical Research Letters*, 40, 3502–3506. <https://doi.org/10.1002/grl.50714>
- Raeder, J. (2006). Flux transfer events: 1. Generation mechanism for strong southward IMF. *Annales de Geophysique*, 24(1), 381–392. <https://doi.org/10.5194/angeo-24-381-2006>
- Russell, C. T., Anderson, B. J., Baumjohann, W., Bromund, K. R., Dearborn, D., Fischer, D., et al. (2014). The Magnetospheric Multiscale magnetometers. *Space Science Reviews*, 199(1–4), 189–256. <https://doi.org/10.1007/s11214-014-0057-3>
- Russell, C. T., & Elphic, R. C. (1978). Initial ISEE magnetometer results—Magnetopause observations. *Space Science Reviews*, 22(6), 681–715. <https://doi.org/10.1007/BF00212619>
- Scholer, M. (1988). Magnetic flux transfer at the magnetopause based on single X-line bursty reconnection. *Geophysical Research Letters*, 15(4), 291–294. <https://doi.org/10.1029/GL015i004p00291>
- Scholer, M. (1995). Models of flux transfer events. In P. Song, B. U. Ö. Sonnerup, & M. F. Thomsen (Eds.), *Physics of the Magnetopause*, *Geophys. Monogr. Ser.* (Vol. 90, pp. 235–245). Washington, DC: American Geophysical Union.
- Shay, M. A., Phan, T. D., Haggerty, C. C., Fujimoto, M., Drake, J. F., Malakit, K., et al. (2016). Kinetic signatures of the region surrounding the X line in asymmetric (magnetopause) reconnection. *Geophysical Research Letters*, 43, 4145–4154. <https://doi.org/10.1002/2016GL069034>
- Sibeck, D. G., Baumjohann, W., & Lopez, R. E. (1989). Solar wind dynamic pressure variations and transient magnetospheric signatures. *Geophysical Research Letters*, 16(1), 13–16. <https://doi.org/10.1029/GL016i001p00013>
- Sibeck, D. G., Kuznetsova, M., Angelopoulos, V., Glaßmeier, K.-H., & McFadden, J. P. (2008). Crater FTEs: Simulation results and THEMIS observations. *Geophysical Research Letters*, 35, L17S06. <https://doi.org/10.1029/2008GL033568>
- Sibeck, D. G., & Siscoe, G. L. (1984). Downstream properties of magnetic flux transfer events. *Journal of Geophysical Research*, 89, 10,709–10,715. <https://doi.org/10.1029/JA089iA12p10709>
- Sibeck, D. G., & Smith, M. F. (1992). Magnetospheric plasma flows associated with boundary waves and flux transfer events. *Geophysical Research Letters*, 19(19), 1903–1906. <https://doi.org/10.1029/92GL01614>
- Siscoe, G. L., & Suey, R. W. (1972). Significance criteria for variance matrix applications. *Journal of Geophysical Research*, 77(7), 1321–1322. <https://doi.org/10.1029/JA077i007p01321>
- Sonnerup, B. U. Ö. (1979). Magnetic field reconnection. In L. J. Lanzerotti, C. F. Kennel, & E. N. Parker (Eds.), *Solar System Plasma Physics* (Vol. 3, pp. 45–108). New York: North-Holland.
- Sonnerup, B. U. Ö., Paschmann, G., Papamastorakis, I., Sckopke, N., Haerendel, G., Bame, S. J., et al. (1981). Evidence for magnetic field reconnection at the Earth's magnetopause. *Journal of Geophysical Research*, 86(A12), 10,049–10,067. <https://doi.org/10.1029/JA086iA12p10049>
- Southwood, D. J., Farrugia, C. J., & Saunders, M. A. (1988). What are flux transfer events? *Planetary and Space Science*, 36(5), 503–508. [https://doi.org/10.1016/0032-0633\(88\)90109-2](https://doi.org/10.1016/0032-0633(88)90109-2)
- Varsani, A., Owen, C. J., Fazakerley, A. N., Forsyth, C., Walsh, A. P., André, M., et al. (2014). Cluster observations of the substructure of a flux transfer event: Analysis of high-time-resolution particle data. *Annales de Geophysique*, 32(9), 1093–1117. <https://doi.org/10.5194/angeo-32-1093-2014>
- Wang, R., Lu, Q., Nakamura, R., Baumjohann, W., Russell, C. T., Burch, J. L., et al. (2017). Interaction of magnetic flux ropes via magnetic reconnection observed at the magnetopause. *Journal of Geophysical Research: Space Physics*, 122, 10,436–10,447. <https://doi.org/10.1002/2017JA024482>
- Wang, R., Lu, Q., Nakamura, R., Huang, C., du, A., Guo, F., et al. (2016). Coalescence of magnetic flux ropes in the ion diffusion region of magnetic reconnection. *Nature Physics*, 12(3), 263–267. <https://doi.org/10.1038/Nphys3578>
- Wang, R., Nakamura, R., Lu, Q., Baumjohann, W., Ergun, R. E., Burch, J. L., et al. (2017). Electron-scale quadrants of the hall magnetic field observed by the Magnetospheric Multiscale spacecraft during asymmetric reconnection. *Physical Review Letters*, 118(17), 175101. <https://doi.org/10.1103/PhysRevLett.118.175101>
- Zhang, H., Khurana, K. K., Kivelson, M. G., Angelopoulos, V., Pu, Z. Y., Zong, Q.-G., et al. (2008). Modeling a force-free flux transfer event probed by multiple Time History of Events and Macroscale Interactions During Substorms (THEMIS) spacecraft. *Journal of Geophysical Research*, 113, A00C05. <https://doi.org/10.1029/2008JA013451>
- Zhong, J., Pu, Z. Y., Dunlop, M. W., Bogdanova, Y. V., Wang, X. G., Xiao, C. J., et al. (2013). Three-dimensional magnetic flux rope structure formed by multiple sequential X-line reconnection at the magnetopause. *Journal of Geophysical Research: Space Physics*, 118, 1904–1911. <https://doi.org/10.1002/jgra.50281>
- Zhou, M., Berchem, J., Walker, R. J., el-Alaoui, M., Deng, X., Cazzola, E., et al. (2017). Coalescence of macroscopic flux ropes at the subsolar magnetopause: Magnetospheric Multiscale observations. *Physical Review Letters*, 119(5), 055101. <https://doi.org/10.1103/PhysRevLett.119.055101>